DYNAMICAL SYSTEMS CHARACTERISATION AND REDUCED ORDER MODELLING OF THERMOACOUSTICS IN A LEAN DIRECT INJECTION (LDI) HYDROGEN COMBUSTOR

Ankit D. Kumar[1,*], Chinonso Ezenwajiaku[2,*], Ramanarayanan Balachandran[2], Andrea Ducci[2], Midhat Talibi[2], James C. Massey[1,3], Nedunchezhian Swaminathan[1]

[1]Department of Engineering, University of Cambridge, Trumpington Street, Cambridge CB2 1PZ, United Kingdom
[2]Department of Mechanical Engineering, University College London, London, WC1E 7JE, United Kingdom
[3]Robinson College, University of Cambridge, Grange Road, Cambridge CB3 9AN, United Kingdom

ABSTRACT

Hydrogen is a promising zero-carbon fuel for decarbonised energy and transportation sectors. While carbon emission is not a concern for hydrogen combustion, its higher adiabatic flame temperature poses challenges of mitigating thermal NO_x *emissions. The wide flammability limits of hydrogen allow a fuel-lean operation, which can reduce* NO_x *emissions. However, lean operation makes the combustion chamber susceptible to thermoacoustic oscillations. In this study, the thermoacoustic instabilities of partially premixed hydrogen flames in a lean direct injection (LDI) multi-cluster combustor are characterised using dynamical systems theory. The combustor was operated at a range of bulk velocities (30 - 90 m/s) and equivalence ratios(0.2-0.6), and time-resolved pressure oscillations and integrated OH* chemiluminescence measurements were taken. The thermoacoustic system reveals a variety of dynamical states in pressure such as period-1 Limit Cycle Oscillation (LCO) with a single characteristic frequency, period-2 LCO with two characteristic frequencies, intermittent, quasi-periodic and chaotic states as either bulk velocity or equivalence ratio is varied. At a bulk velocity of 30 m/s, as the equivalence ratio is gradually decreased from 0.6 to 0.2, the dynamical behaviour follows a sequence from an intermittent state to a period-1 LCO, then to a quasi-periodic state, and eventually reaches a chaotic state. As the equivalence ratio is decreased for a bulk velocity of 60 m/s, the pressure oscillations evolve from a period-2 LCO to quasi-periodic state before flame blows off. The emergence of period-2 and quasi-periodic states indicates the presence of strong non-linear interactions among the cavity acoustic modes. These modes and their spatial behaviour are investigated using a reduced order model which solves the 3D inhomogeneous Helmholtz equation with an n-tau flame model. The analyses show that the period-2 and quasi-periodic states can arise due to the interaction between the plenum and combustion chamber modes indicating that hydrogen flames may excite a wide range of cavity acoustic modes.*

Keywords: Hydrogen, Thermoacoustic instability, Lean Direct Injection (LDI), Dynamical systems characterisation, Reduced Order Modelling (ROM)

1. INTRODUCTION

The pursuit of decarbonisation has intensified interest in hydrogen combustion. While several recent studies have focused on the combustion characteristics of hydrogen-hydrocarbon fuel blends [1–4], only few studies have addressed the challenges in pure hydrogen combustion. The primary challenges of hydrogen combustion are flashback, NO_x emissions and thermoaocustic instabilities. It is imperative that the combustor configuration is essential in overcoming these challenges. Lean fully premixed configuration allows combustion at very low mean temperatures which abates NO_x emissions but the homogeneous lean fuel-air mixture promotes flame flashback and combustion instabilties [5, 6]. Partially premixed swirl stabilisation is a popular approach for natural gas combustion which offer flexibility to operate with hydrogen-natural gas blends. However, the efficient mixing capabilities of swirl stabilised configurations make it susceptible to flashback and thermoacoustic instabilities at higher hydrogen content. Micromix combustion configuration is also a promising approach to mitigate NO_x emissions by lowering the mixing residence time, but the high wall temperatures associated with this configuration can damage the nozzle [7]. An alternative approach is Lean Direct Injection (LDI) which is considerably more resistant to flame flashback than the other configurations. The flashback resistance of LDI is primarily achieved by directly injecting fuel and air through separate streams into the combustion chamber.

Past studies on LDI concept have focused on flashback, NO_x emissions and combustion efficiency [8, 9]. Flashback events are less likely for such a configuration even for adiabatic flame temperatures as high as 1900 K [8], however NO_x emissions increased by 6 ppm compared to its premixed counterpart. It was shown in Ref. [9] that hydrogen combustion in various LDI con-

*Corresponding author: adk46@cam.ac.uk,chinonso.ezenwajiaku@ucl.ac.uk
Documentation for `asmeconf.cls`: Version 1.35, July 19, 2024.

figurations emits up to 5 times lower NO_x emissions compared to Jet-A fuel in the same set of configurations. However, thermoacoustic instabilities, which result from the positive coupling between heat release rate and acoustic waves, have not received much attention in the context of 100% hydrogen combustion in an LDI combustor. Therefore, a complete characterisation of thermoacoustic instabilities for such a configuration is important to enable future studies on instabilities and their control.

Thermoacoustic instabilities in gas turbine combustors produce large pressure oscillations causing high thermal loads and structural fatigue that compromise the combustor life. These instabilities have received considerable attention in the combustion community especially for conventional hydrocarbon fuels like natural gas [10, 11]. Recent interest in blended hydrogen-natural gas combustion has led to several studies on thermoacoustic instabilities for these blended fuels [2, 3, 12]. However, very few studies have focused on these instabilities for 100% hydrogen combustion [6, 13].

Addition of H_2 has shown to excite higher acoustic modes and also result in nonlinear interactions between these modes [3, 6, 12, 13]. The dynamical state of the combustion instability is not limited to classical period-1 Limit Cycle Oscillation (LCO) in the presence of nonlinear interactions. For instance, nonlinear interaction between two acoustic modes can result in period-2 thermoacoustic oscillations [12, 14]. More complex dynamical states may arise such as quasi-periodic, period–κ ($\kappa > 2$, is the least common integer multiple of two independent unstable mode frequencies), intermittency and chaotic states [15]. A comprehensive characterisation of such dynamical states in thermoacoustic systems have been performed extensively in the past [16–18]. Several dynamical states such as period-2, quasi-periodic states were recognised in a ducted laminar flame [16] using tools from dynamical systems theory. However, such a wide range of dynamical states have not been observed and characterised in 100% hydrogen combustion in an LDI configuration. The presence of such complex dynamical states renders single mode control obsolete and active control using variable frequency external forcing may become important [19].

Dynamical characterisation of thermoacoustic instabilities is an important step before one can proceed to model the system to enable prediction and control. Prediction and control of thermoacoustic instabilities requires a reliable and accurate modelling framework. Thermoacoustic instabilities are often modelled as a system of multiple nonlinear oscillators such as Stuart-Landau oscillators, Van der Pol oscillators and so on [20]. Such a framework usually involves a set inhomogeneous partial differential equations where the homogeneous part closely resembles the Helmholtz equation for linear acoustics and the inhomogeneous part encompasses the nonlinearities arising from the flame dynamics. Before establishing such a framework one must answer several questions, such as (i) How many Degrees of Freedom (DoF) does the system possess? (ii) Can the system be approximated as a quasi-linear system ignoring nonlinearities? (iii) If the system is nonlinear, what form of nonlinearity (cubic, quadratic, etc.) best approximates the system? (iv) How many acoustic modes are sufficient to model the dynamics? Tools from dynamical systems theory and nonlinear time series analysis are particularly useful in answering these questions.

TABLE 1: SUMMARY OF THE CONSIDERED EXPERIMENTAL CASES.

Case	ϕ	U_b(m/s)	Case	ϕ	U_b(m/s)
1a	0.2	30	2a	0.2	60
1b	0.3	30	2b	0.3	60
1c	0.4	30	2c	0.4	60
1d	0.5	30	2d	0.5	60
1e	0.6	30	2e	0.6	60

It is important to note that linear frameworks are not completely obsolete in the face of complex dynamical states. Reduced Order Modelling (ROM) using linear flame models recovers spatial information of thermoacoustic mode which is absent in nonlinear time series analysis. The spatial information is important to identify key locations where passive or active control strategies can be optimally applied [21–23]. Furthermore, spatial characteristics are key to identify nature of the modes especially in the presence of multiple unstable modes that are interacting. In this work, tools from dynamical systems theory and ROM are used to analyse the temporal and spatial characteristics of thermoacoustic instabilities of pure hydrogen combustion in an LDI combustor. Such an analysis offers insights into the spatio-temporal characteristics of a peculiar interaction between two unstable modes that results in a *beating* phenomena.

This article is organised as follows. A brief description of the experimental method and test cases are presented in the next section. The results pertaining to dynamical systems characterisation are described in section 3. Results of the ROM are discussed in section 4. The conclusions are summarised in section 5.

2. GEOMETRY AND CASES

A detailed description of the experimental facility can be found in Ref. [24]. For this study, a total of 10 cases listed in Tab. 1 are analysed. These cases are at two bulk mean velocities (determined at the exit of the injector plate, [24]) $U_b = 30$ m/s and $U_b = 60$ m/s across 5 global equivalence ratios ϕ ranging from 0.2 to 0.6. All measurements were performed at atmospheric conditions of temperature and pressure for air and H_2.

A schematic of the simplified geometry used for ROM is shown in Fig. 1. The geometry comprises of a long plenum connected to a combustion chamber downstream through a mixing/injection tube. The upstream and downstream reflection coefficents are denoted by $\mathcal{R}_{in}$ and $\mathcal{R}_{out}$ respectively, which are given in Eq. (8) in section 4.

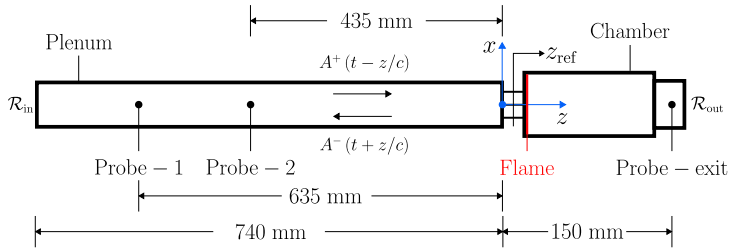

FIGURE 1: SCHEMATIC OF THE GEOMETRY.

3. DYNAMICAL SYSTEMS CHARACTERISATION

3.1 Time-series

Figure 2 shows the time series of pressure fluctuations (p') at probe-2 and the corresponding amplitude Probability Density Function (PDF) for all the cases. At $U_b = 30$ m/s, pressure fluctuations with large amplitude are seen for all cases except case 1a ($\phi = 0.2$, $U_b = 30$ m/s). Interestingly, case 1b is composed of significant amplitude modulation resembling *beating* phenomenon. Case 1c and 1d resemble a period-1 LCO which will be confirmed in the next subsection. Case 1e shows a complex LCO which needs further assessment to be completely characterised. The amplitude of p' increases gradually as the global equivalence ratio is decreased from 0.6 to 0.4. Upon further reduction ϕ, first the amplitude drastically increases (at $\phi = 0.3$) and then sharply decreases (at $\phi = 0.2$).

The amplitude PDFs (constructed from the time series) show a distribution of the local stationary points (maxima and minima). The PDFs show a wide variety of shapes including normal, bimodal and nearly uniform distribution. Case 1a has a normal distribution and its low-amplitude leads to the conclusion that it may be stable. It is quite likely that this signal is also chaotic which will be confirmed in the next subsection. Given the substantial amplitude modulation which is clearly visible in the time series of p' for case 1b, it is expected to have a broad and nearly uniform PDF as seen in Fig. 2. Case 1c and 1d show a bimodal PDF which is slightly asymmetric. It was observed in a past study that the asymmetry is a result of nonlinear contributions from higher acoustic modes [25]. Therefore, these PDFs are a first indication of nonlinear interaction between higher acoustic modes. The asymmetry is also a result of time-delay which are routinely found in thermoacoustic systems. Case 1e shows an asymmetric amplitude PDF suggestive of strong nonlinear interactions with higher acoustic modes.

At $U_b = 60$m/s, cases 2c, 2d and 2e show a non-monotonic amplitude behaviour along with a peculiar LCO behaviour. At $\phi = 0.3$, amplitude modulation similar to case 1b is observed before flame blow off occurs at $\phi = 0.2$. The amplitude PDFs show a trimodal behaviour for cases 2c, 2d and 2e. The PDFs are assymmetric for cases 2d and 2e whereas case 2c shows a symmetric PDF. This indicates a stronger contribution from higher harmonics in cases 2d and 2e compared to case 2c [25]. Such trimodal PDFs are rarely seen in the literature and is an indication of multiple degrees of freedom of the dynamical system or in other words that acoustic energy is distributed across multiple acoustic modes. The amplitude modulation in case 2b results in a broad distribution of probabilities. Since the flame has blown-off for case 2a, the pressure fluctuations are negligible.

3.2 Frequency spectra

It is interesting to analyse the frequency spectrum of the Sound Pressure Level (SPL) at probe-2. The SPL is defined as

$$\mathrm{SPL}(f) = 10\log_{10}\left(S_{p'p'}\right), \tag{1}$$

where $S_{p'p'}$ is the Power Spectral Density (PSD) of normalised pressure fluctuations p'/p_{ref} obtained using Welch's method with 4 Hanning windows and 50% overlap, and the reference pressure $p_{\mathrm{ref}} = 20\mu$Pa. The values of the dominant peak frequencies for all cases are listed in Tab. 2. The SPL for cases 1b and 1e shown in Fig. 3 show multiple peaks at frequencies which are linear combinations of two independent frequencies f_0 and f_1. Since these two frequencies are incommensurate, that is they are not in whole number proportions, the constituent oscillations are of quasi-periodic nature. Quasi-periodic oscillations are *almost* periodic oscillations even in the absence of turbulence/stochastic noise and in the limit of infinite time-period. Cases 1c and 1d show multiple peaks but the peak at $f_1 = 2f_o$ could be a harmonic (integral multiple of the fundamental frequency) resulting from quadratic nonlinearity . For instance, if $\dot{Q}' \propto \dot{p}'^2$ [25] then using the ansatz $\dot{p}' \sim |\hat{p}|\exp(-2\pi i f_0 t)$, one can see that peaks at $2f_o$ may arise. Interestingly, higher acoustic modes can contribute to the overall acoustic energy even if they are stable [25]. Case 1a shows no peaks above 80 dB and has a broadband spectrum, which is a characteristic of chaotic signals.

TABLE 2: DOMINANT FREQUENCIES (IN HZ) IN EACH CASE.

Case	f_0	f_1	Case	f_0	f_1
1a	-	-	2a	-	-
1b	128	791	2b	94	820
1c	928	1856	2c	960	1920
1d	942	1884	2d	996	1992
1e	75	1042	2e	1002	2004

Cases 2d and 2e have an interesting spectrum where $f_0 = f_1/2$, but it is not the fundamental frequency, that is, the frequency with maximum SPL. Frequencies which are integral submultiples of the fundamental frequency, or in other words, proportional to f_1/r where r is any integer, are called subharmonics. Therefore, cases 2d and 2e feature subharmonics at f_0 and are quite likely to be period-2 oscillations. Note that these are not characterised as quasi-periodic oscillations because the peak frequencies are commensurate. Case 2c shows two dominant peaks at commensurate frequencies, however there are no subharmonics and further analysis is required to characterise them as either period-1 or period-2. Case 2b shows a quasi-periodic oscillation with two independent frequencies at f_0 and f_1 before blow-off occurs for case 2a.

3.3 Nonlinear Time-Series Analysis

The frequency spectra has allowed to recognise some dominant frequencies in the system. However, the DoF of a complex system cannot be discerned from the spectra. Tools from nonlinear time-series analysis overcome this limitation. To proceed with it, the discrete pressure time-series is mapped onto a higher-dimensional vector space as follows

$$\boldsymbol{\xi}(t_\iota) = [p'(t_\iota), p'(t_\iota - \tau), \cdots, p'(t_\iota - (m-1)\tau)], \tag{2}$$

where τ is an appropriate time delay, m is the embedding dimension of the phase space and $\iota = 1, 2, \cdots, N - (m-1)\tau$ for a total N data points in the time-series. Such a reconstruction produces a phase space of time-delayed coordinates as in Eq. (2). The time-series can then be visualised in this higher-dimensional (m) phase space which allows extraction of its topological features. Based on these features the system can then be uniquely characterised into standard dynamical states such as period-1, period-2, quasi-periodic, chaotic and so on, which is one of the primary objectives of this work. As mentioned previously in section 1, such

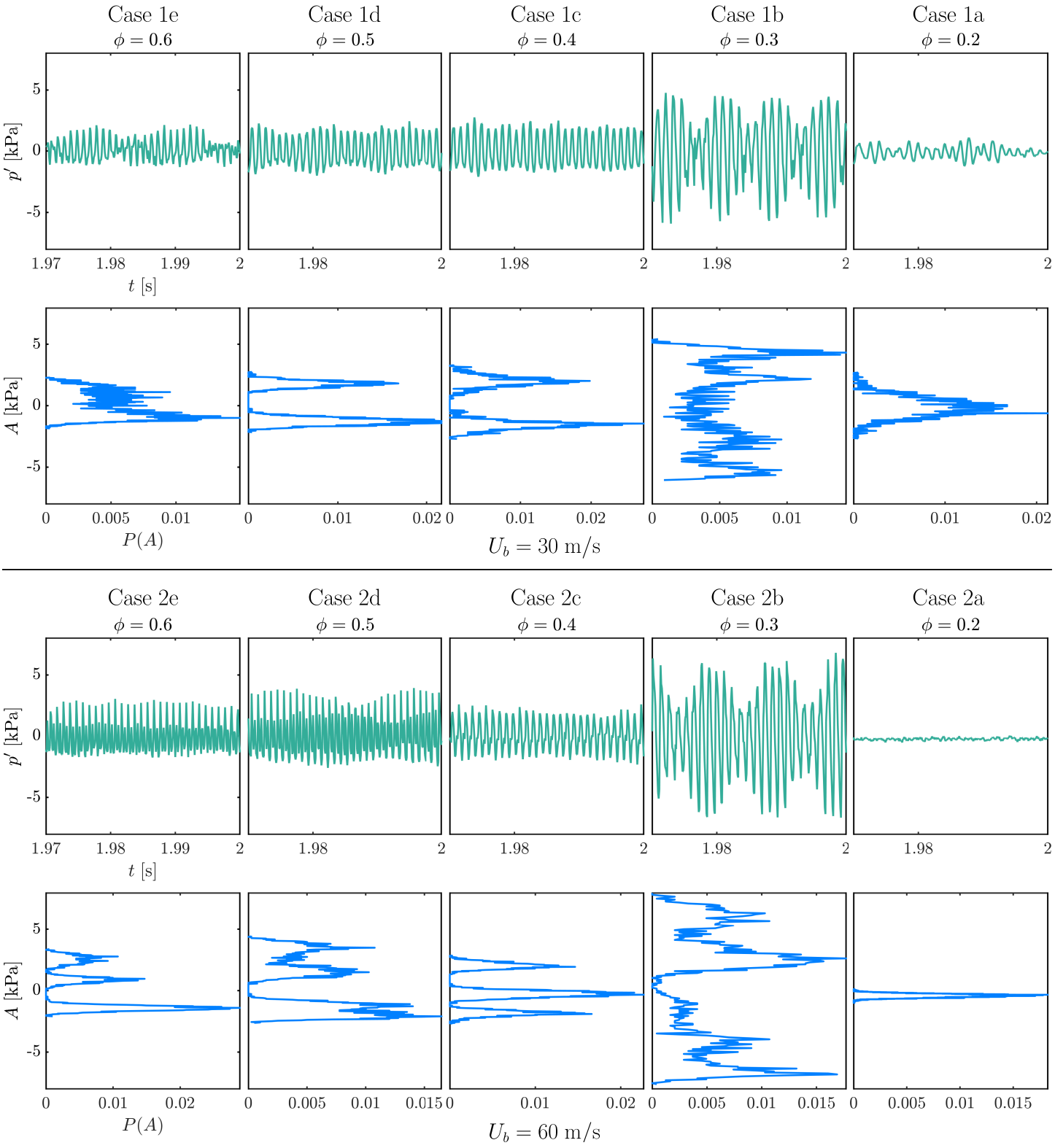

FIGURE 2: PRESSURE TIME SERIES AND AMPLITUDE PDFS AT PROBE-2 FOR U_b = 30M/S (TOP TWO FRAMES) AND U_b = 60 M/S (BOTTOM TWO FRAMES).

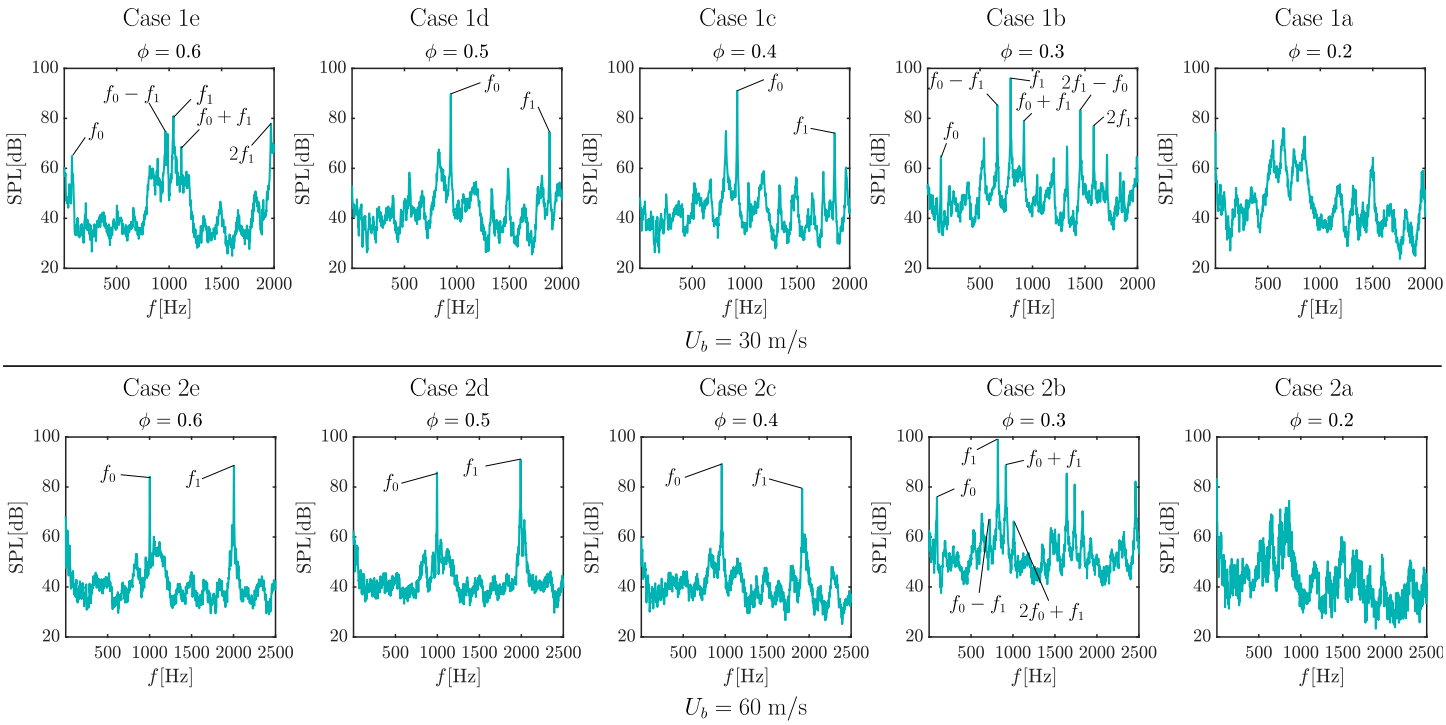

FIGURE 3: FREQUENCY SPECTRUM OF SPL AT PROBE-2 FOR U_b = 30M/S (TOP FRAME) AND U_b = 60 M/S (BOTTOM FRAME).

a characterisation is essential to decide the appropriate modelling framework.

The optimal time delay will maximise the one-to-one correspondence between the pressure time-series in the original space and the reconstructed phase space. In this work, the first local minimum of the Average Mutual Information (AMI) [26] is used to choose the optimal time-delay. More details on AMI can be found in [14, 15]. The embedding dimension m for the reconstructed phase space needs to be high enough to avoid false crossings in the phase space. This means that the neighbouring points of each trajectory in an m–dimensional space should be identical to those in an $m-1$ phase space. The value of m which gives a near zero percentage of false neighbours, evaluated using the False Nearest Neighbours (FNN) method [27], is considered the minimum embedding dimension. Applying this method, the minimum dimension of 3 is found to be suitable to resolve the main features of the dynamics for most cases. This is quite convenient for a qualitative 2D $(m-1)$ representation using a Poincaré map. For the evaluation of more quantitative information shown later, such as the correlation dimension (D_c) which is closely related to the DoF of the system, higher values of m are used to achieve better convergence.

For brevity, the characterisation of the system is made using only the Poincaré map which are transverse cuts of the phase space plot of $\boldsymbol{\xi}(t_\iota)$. Therefore, the Poincaré map reduces the dimension of the phase space plot from m to $m-1$ making it convenient for visualisation. For instance, a phase space of dimension $m = 3$ would be represented by a 3D plot of $\boldsymbol{\xi}(t_\iota) = [p(t_\iota), p(t_\iota - \tau), p(t_\iota - 2\tau)]$ and its Poincaré map, which is a 2D representation in this case, would be a transverse cut of the 3D plot. A Poincaré map (see Fig. 4) can then be used to identify the different dynamical states based on their topological features. A chaotic state or thermoacoustically stable state shows a random scatter of points around the origin in both the 3D phase space and the Poincaré map. A period-1 and period-2 oscillation form a single and double loop attractor respectively in the 3D phase space. The corresponding Poincaré map features one cluster for period-1 state and 2 clusters for period-2 state. A quasi-periodic oscillation forms a torus in the 3D phase space which corresponds to a loop in the Poincaré map. The torus is essentially a thick loop where the thickness is a result of the oscillations being *almost* periodic. Therefore, the loop drifts within the volume of a torus over time and this is irrespective of the presence of turbulence/stochastic noise.

The mean D_c of a time-series data is an indicator of the number of active DoF of a system. Mathematically, it is also a measure of the self-similarity in a system. It takes a value of 0 for a steady state, 1 for a periodic oscillation of any period, 2 for a quasi-periodic oscillation, a finite non-integer value for a deterministically chaotic process and a very large value that tends towards infinity for a stochastic (random) process. However, in the presence of significant turbulence resulting in broadband fluctuations, the D_c value can deviate from these values to take non-integer values. In the presence of turbulence, filtering the signal using a phase preserving filter and using global quantities for the characterisation of the system may be useful [28]. The mean D_c is given by

$$\overline{D_c(m,R)} = \overline{\frac{\partial \log C(m,R)}{\partial \log R}}, \tag{3}$$

where D_c is the logarithmic slope of the correlation sum $C(m,R)$ over a range of radii R for an embedding dimension m. The

correlation sum is the mean probability that two states at different times $\xi(t_\iota)$ and $\xi(t_j)$ are within a certain Euclidean distance R. It is evaluated as follows

$$C(m,R) = \lim_{N\to\infty} \frac{1}{N_{\text{pair}}} \sum_{i,j=1,i\neq j}^{N-(m-1)\tau} \Theta\left(R - \|\xi(t_\iota) - \xi(t_j)\|\right), \quad (4)$$

where $N_{\text{pair}} = (N-(m-1)\tau-1)(N-(m-1)\tau)/2$ is the number of non-repeating pair of points, Θ is the Heaviside step function and in case of a finite number of data points, N should be sufficiently large as in this study with over 10,000 points. The Euclidean distance between two points, $\xi(t_\iota)$ and $\xi(t_j)$, in the phase space is given by

$$\|\xi(t_\iota) - \xi(t_j)\| = \sqrt{\sum_{l=0}^{m-1} \left(p'(t_\iota - l\tau) - p'(t_j - l\tau)\right)^2}. \quad (5)$$

The top row of Fig. 4 shows the Poincaré map for $U_b = 30$ m/s. The Poincaré map which is a cut section of the 3D phase portrait of $p(t_\iota), p(t_\iota - \tau), p(t_\iota - 2\tau)$ can also be constructed as a scatter plot of successive local maxima of the pressure time series signal. For case 1a at $\phi = 0.2$, the map reveals a cluster which is close to $p'_{\text{max}} \approx 0$, suggesting a stable or chaotic state. Increasing the equivalence ratio to $\phi = 0.3$ results in a quasi-periodic oscillation characterised by the single loop centred on the bisectrix in the Poincaré map. This loop is well away from the origin given the high amplitude oscillation. Further increasing the equivalence ratio results in a single cluster on the bisectrix resulting from a period-1 oscillation. The clusters also move closer to the origin indicating a decreasing amplitude upon increasing equivalence ratio. Case 1e at $\phi = 0.6$ shows on elongated cluster along the bisectrix and no discernible cluster or loop is visible which happens when the embedding dimension is much higher than the dimension used for visual representation [20]. Turbulence in the system acts to add noise in the dynamics which results in the scatter in both clusters and loops.

The bottom frame of Fig. 4 shows the correlation dimension which is a measure of the number of active DoF of the system. Case 1e shows that D_c for the unfiltered signal is $\gtrapprox 4$ while the filtered signal is $\gtrapprox 3$, suggesting that the system dynamics is complex with a considerable impact of stochastic noise arising from turbulence. The filtering operation has a low-pass phase-preserving behaviour with a cutoff frequency of 1000 Hz and the resulting D_c is significantly different from the unfiltered signal indicating the importance of the higher harmonics in the system dynamics. The filtering operation also allows to isolate the effect of high-frequency broadband fluctuations. The high D_c value for this case also explains the reasons for its higher embedding dimension which evaded appropriate visualisation on a 2D Poincaré map. The frequency spectrum for this case had features of a quasi-periodic oscillation and its high D_c value indicates that this case could be a case of a noisy or intermittent quasi-periodic oscillation [28]. These observations offer insights into the appropriate modelling framework required. For instance, the high D_c value along with asymmetric amplitude PDF seen in Fig. 2 indicates that the model will require at least 3-4 governing equations each corresponding to an acoustic mode. The quasi-periodic nature enables us to recognise at least two unstable modes and since $D_c > 2$, a significant level of stochastic forcing may be necessary.

The correlation dimension for cases 1c and 1d approach a mean value of approximately 1 in the regime $0.6 < R/R_{\text{max}} < 1$, indicating a periodic oscillation and confirming the qualitative conclusions of the 2D Poincaré map. In case 1b, the unfiltered signal indicates a mean correlation dimension $\overline{D_c} \approx 3$ for $0.3 < R/R_{\text{max}} < 0.6$ and $2 < \overline{D_c} < 3$ for $R/R_{\text{max}} > 0.6$. The filtered signal shows slightly lower values of D_c (between 2 and 3) at small scales, indicating a quasi-periodic oscillation. At large scales, the filtered system approaches a periodic behaviour since $1 < D_c < 2$. The values of D_c are not precisely equal to integer values which indicates the effect of intermittency or noise. Further study on the presence and influence of intermittency is beyond the scope of the current work and will be explored in a future study. The different $\overline{D_c}$ values at large and small scales indicates a scale separation occurring in the phase space. This is due to a disparity in the major and minor radius of the torus corresponding to the quasi-periodic oscillation in the phase space (not shown) [20]. Case 1a shows very high values of D_c with a large scatter indicating the presence of chaotic dynamics.

Figure 5 shows the Poincaré map and the variation of correlation dimension with normalised Euclidean distance (in phase space) for $U_b = 60$ m/s. The off-diagonal clusters in cases 2d and 2e indicate a period-2 oscillation. Case 2c shows 3 clusters, but this does not indicate a period-3 oscillation since one of the clusters is on the bisectrix similar to a period-1 oscillation. Therefore, the system intermittently switches between period-1 and period-2. Note also that the frequency spectrum showed no evidence of a third period. Case 2b is very similar to case 1b showing a loop centred on the bisectrix which indicates the presence of a quasi-periodic oscillation. Blow-off has occurred for Case 2a so no meaningful dynamics may be identified. The correlation dimension for cases 2c, 2d and 2e all show a mean value of 1 at intermediate scales indicating the presence of a periodic oscillation. Note that the correlation dimension of periodic oscillations of any period are indistinguishably close to a value of 1. The correlation dimension for case 2b is similar to case 1b showing a two self-similar scales.

4. REDUCED ORDER MODELLING (ROM)

While nonlinear time-series analysis was useful in identifying the essential temporal features required to model the thermoacoustic system, spatial information of the modes is unavailable. Therefore, an open source 3D Helmholtz solver JULHOLTZ [29] is used to estimate unstable modes and their spatial features. In this approach, the thermoacoustic modes are obtained from the solution of the following equation

$$\nabla \cdot \left(\overline{c}^2 \nabla \hat{p}\right) + s_k^2 \hat{p} = -i s_k (\gamma - 1)\hat{Q}, \quad (6)$$

where $\overline{c}$ is the mean speed of sound, s_k is eigenvalue of mode k, γ is the ratio of specific heat capacities and $i = \sqrt{-1}$. The quantities $\hat{p}$ and $\hat{Q}$ are Fourier-transformed pressure and volume-integrated heat release rate fluctuations. The flame response is often related to the velocity fluctuations at a reference axial location z_{ref} (see

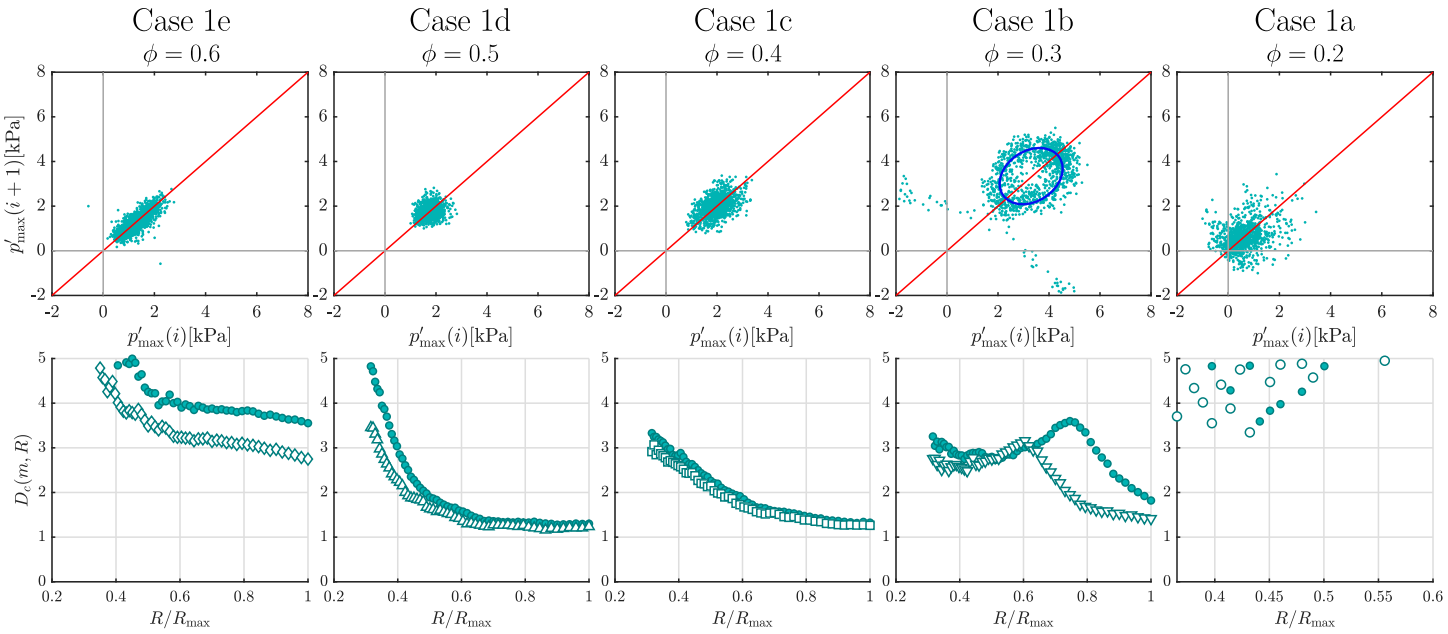

FIGURE 4: POINCARÉ SECTION (TOP FRAME) AND SLOPE OF THE CORRELATION SUM D_c FOR A RANGE OF NORMALISED EUCLIDEAN DISTANCE $R/R_{\max}$ FOR U_b = 30 M/S. THE FILLED SYMBOLS IN THE BOTTOM FRAME CORRESPOND TO UNFILTERED SIGNAL WHEREAS THE OPEN SYMBOLS CORRESPOND TO LOW PASS FILTERED SIGNAL WITH A SUITABLE CUTOFF FREQUENCY TYPICALLY OF THE ORDER OF 1000 HZ. THE RED LINE DENOTES THE BISECTRIX AND THE GREY LINES DENOTE $p'_{\max}(i) = 0$ AND $p'_{\max}(i+1) = 0$ LINES.

Fig. 1) using the familiar n–τ model given by [30]

$$\hat{Q} = n \exp(-is_k\tau)\nabla\hat{p}|_{z_{\text{ref}}} \cdot \widehat{j}_{z\text{ref}}, \tag{7}$$

where n is the interaction index, τ is the time delay (not to be confused with τ) between the velocity fluctuations at the reference location and the heat release rate, and $\widehat{j}_{z\text{ref}}$ is the unit vector in the axial direction at the location $(0, 0, z_{\text{ref}})$. Equations (1) and (2) constitute an eigenvalue problem whose solution gives a complex eigenvalue (also known as a mode) $s_k \equiv 2\pi(f_k - ig_k)$ (for the ansatz $\hat{p} \sim \exp(is_k t)$) where f_k is the frequency and g_k is the growth rate.

The computational domain is discretised using 73,000 tetrahedral cells for the ROM. The mean speed of sound in the entire domain takes either the unburnt mixture value $\overline{c}_u$ upstream of the flame or the burnt mixture value $\overline{c}_b$ downstream of the flame. The speed of sound is obtained using the relation $\overline{c} = \sqrt{\gamma\mathscr{R}T}$, where $\mathscr{R}$ is the universal gas constant, temperature T takes either the unburnt mixture value T_u upstream of the flame or is approximated using the adiabatic flame temperature T_b downstream of the flame and $\gamma \approx 1.4$. These approximations are routinely used in reduced order models [29] and are reasonable since the eigenmode frequencies and growth rates are seen to be fairly insensitive to small variations ($\sim$ 100 K) in temperature. The eigenvalues of Eq. (6) for the burner are obtained using JULHOLTZ for both an unexcited cavity (in the absence of the flame) and for a range of n–τ values. The flame is assumed to be thin and located at the dump-plane. The inlet boundary condition corresponding to zero velocity fluctuations is specified with $\nabla\hat{p} = 0$, since the mass flow is constant at the inlet. High frequency acoustic waves may, however, modulate the mass flow rate quicker than the response time of the mass flow controller. Parametric variation of the inlet reflection coefficient reveals no appreciable change in the eigenvalues and hence $\nabla\hat{p} = 0$ is specified. For instance, $\mathcal{R}_{\text{in}} = 1, 0.5$ and $0.5 + i$ yield eigenvalues that differ by at most 0.015% for the parametric combination $[n, \tau, \mathcal{R}_{\text{out}}] = [0.3, 1\text{ms}, -0.3]$. The negligible sensitivity results from the presence of a velocity node at the inlet for all parametric combinations. The inlet is therefore assumed to be perfectly reflecting with a reflection coefficient of $\mathcal{R}_{\text{in}} = 1$, where the reflection coefficient $\mathcal{R}$ is defined in terms of characteristic wave amplitudes $A^{\pm}$ as

$$\mathcal{R} \equiv \frac{A^+}{A^-},\ A^+ \equiv \frac{1}{2}(p' + \overline{\rho}\,\overline{c}\,u'),\ \text{and}\ A^- \equiv \frac{1}{2}(p' - \overline{\rho}\,\overline{c}\,u') \tag{8}$$

The outlet boundary is open to the atmosphere (where $p' = 0$), but it is not perfectly reflecting because the pressure fluctuations measured at the exit pressure probe is non-zero. Acoustic energy is lost with the mean flow at the outlet and therefore $\mathcal{R}_{\text{out}}$ is treated as a parameter in the absence of further information on the outlet reflection coefficients.

Cases 1b and 2b are considered for comparison of ROM results with measurements. The speed of sound $\overline{c}_b$ corresponding to the adiabatic flame temperature of the mixture at $\phi = 0.3$ is specified downstream of the flame location. In the absence of the flame ($n = 0$), the eigenmodes of the geometry are computed for various outlet reflection coefficients as shown in Fig. 6. All modes recognised in this work are longitudinal acoustic modes. The results reveal that the eigenmode at $f_o = 118$ Hz for the perfectly reflecting case is a plenum mode where the pressure is maximum in the plenum. The eigenmode at $f_1 = 824$ Hz for the perfectly reflecting case corresponds to a higher frequency plenum mode characterised by the four nodes and antinodes of pressure. At $\mathcal{R}_{out} = -1$, the combustion chamber is inactive

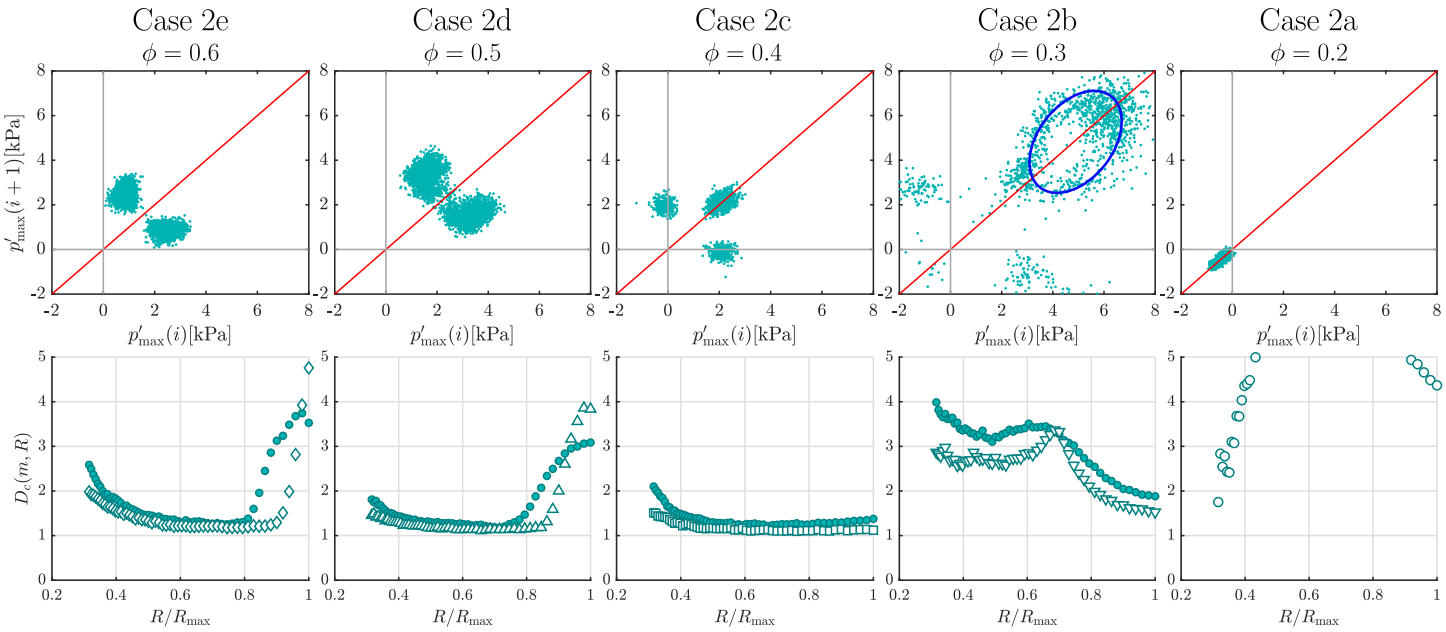

FIGURE 5: FIGURE CAPTION SAME AS FIG. 4 EXCEPT THAT IT CORRESPONDS TO CASE U_b = 60 M/S.

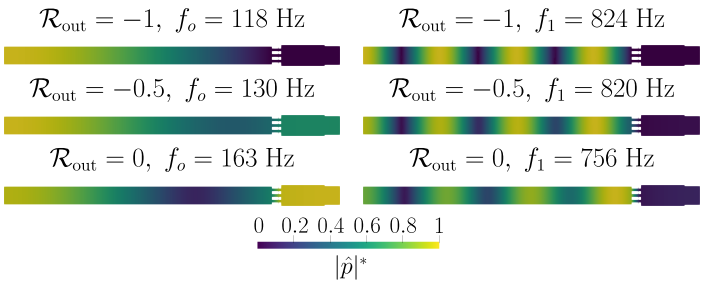

FIGURE 6: ACOUSTIC PRESSURE MODE AMPLITUDES OBTAINED FROM ROM FOR CASE 1B AND 2B IN THE ABSENCE OF A FLAME.

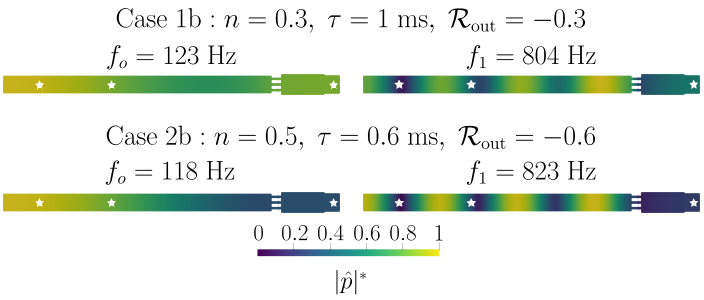

FIGURE 7: ACOUSTIC PRESSURE MODE AMPLITUDES OBTAINED FROM ROM FOR CASE 1B AND 2B IN THE THE PRESENCE OF A FLAME. THE WHITE STAR DEMARCATES THE LOCATION OF THE PRESSURE PROBES.

($|\hat{p}| \approx 0$). Decreasing the outlet reflection coefficient results in the upstream traversal of the pressure node in the plenum. Furthermore, the eigenmode frequency increases and also the pressure amplitude in the chamber. Since the pressure amplitude at the exit probe is non-zero as indicated in Tab. 3, this result provides evidence for choosing an imperfectly reflective outlet boundary in the discussion to follow. The mode shape undergoes a negligible change while the frequency only slightly decreases for the higher frequency f_1 mode at $\mathcal{R}_{\text{out}} = -0.5$. Further decreasing $\mathcal{R}_{\text{out}}$ to obtain a non-reflective outlet results in downstream shifting of the nodes and antinodes. The antinodes are no longer of equal strength and their value increases in the downstream direction. The chamber remains inactive for this mode independent of the outlet reflection coefficient. Since the measured pressure amplitude is non-zero even at f_1, this result is therefore insufficient to explain the experimental observations.

Figure 7 shows the pressure mode shapes for two cases at f_o and f_1 in the presence of flame dynamics ($n \neq 0$). The values of the parameters (n, τ, and $\mathcal{R}_{\text{out}}$) are chosen empirically to match the measured trend in pressure amplitude at the three probe locations (see Tab. 3) of the most energetic mode (f_1). Note that $|\hat{p}|^*$ is normalised by the maximum value in the entire domain whereas $|\hat{p}|^\dagger$ is normalised by the maximum value amongst the three probe values. The frequency f_o obtained from ROM is in good comparison with the measured value for case 1b (see Tab. 2). This mode is a mixed plenum and chamber mode with non-zero pressure amplitude in both the plenum and the chamber mode. The higher frequency f_1 is also in good comparison with the measured value (see Tab. 2). This mode is also a mixed plenum and chamber mode albeit the pressure amplitude in the chamber is not as significant as at f_o. For case 2b, the lower frequency mode f_o is overestimated by about 24 Hz and the characteristics of the mode shape suggest that this mode is a mixed plenum and chamber mode. The chamber pressure is not as high as the case 1b at f_o. Frequency f_1 is in close comparison with the measured value for case 2b and the mode amplitudes are dominant in the plenum compared to the chamber.

These results suggest that the quasi-periodic oscillations observed for cases 1b and 2b are a result of the interaction between the plenum and chamber modes. The linear framework of n–τ

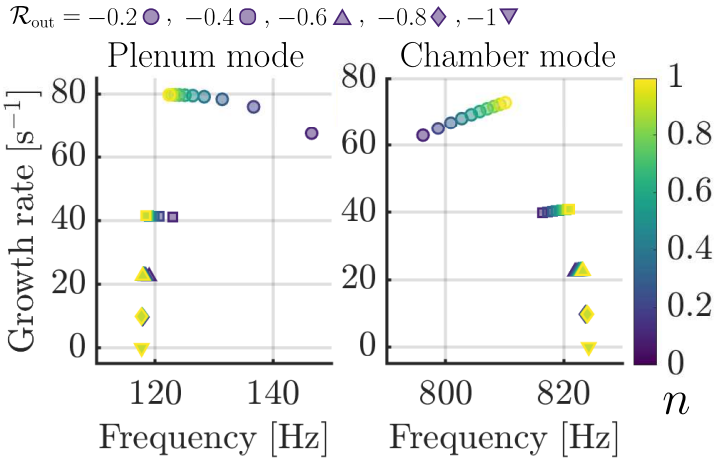

FIGURE 8: THERMOACOUSTIC EIGENVALUE VARIATION WITH $\mathcal{R}_{out}$ AND n FOR THE PLENUM AND THE CHAMBER MODE AT τ = 0.6 ms.

TABLE 3: MEASURED AND COMPUTED (ROM) PRESSURE AMPLITUDES AT f_o AND f_1 ACROSS DIFFERENT PROBE LOCATIONS FOR CASES 1B AND 2B. $|\hat{p}|^{\dagger} = |\hat{p}|/\max\left(|\hat{p}|_1, |\hat{p}|_2, |\hat{p}|_{exit}\right)$

.

		Exp.		ROM	
Case	Probe	$\lvert\hat{p}\rvert^{\dagger}(f_0)$	$\lvert\hat{p}\rvert^{\dagger}(f_1)$	$\lvert\hat{p}\rvert^{\dagger}(f_0)$	$\lvert\hat{p}\rvert^{\dagger}(f_1)$
1b	Probe – 1	1	0.23	1	0.24
	Probe – 2	0.31	0.65	0.85	0.69
	Probe – exit	0.47	1	0.85	1
2b	Probe – 1	1	0.1	1	0.38
	Probe – 2	0.34	1	0.84	1
	Probe – exit	0.51	0.53	0.45	0.94

model allows to capture the right trends in the pressure amplitude shown in Tab. 3 and make accurate estimates of the mode frequencies. There are discrepancies in the quantitative comparisons especially at f_o because the parameters were empirically chosen to match the trend at f_1. Since these parameters are definitely frequency dependent a different choice of parameters at f_1 may yield a better comparison. However, with the lack of a Flame Transfer Function (FTF) and outlet reflection coefficients available from the experiments such an exercise is too tedious.

Figure 8 shows the variation of the eigenvalues with the interaction index n and the outlet reflection coefficient $\mathcal{R}_{out}$. The frequency of the plenum mode decreases whereas an opposite trend is observed for the chamber mode with increasing n. This trend can be explained by closely analysing the mode shapes of the passive modes shown in Fig. 6. Since lower values of $\mathcal{R}_{out}$ show a greater sensitivity, consider the mode shape corresponding to $\mathcal{R}_{out} = 0$ in Fig. 6 for illustration. A pressure node (velocity node) is found upstream and downstream of the flame for plenum and the chamber mode respectively. Since the flame response is proportional to acoustic velocity at the reference location as seen in Eq. 7, the increased interaction index n results in increased velocity at the reference location through the acoustic feedback characterised by Eq. 6. The increased velocity at the reference location just upstream of the flame effectively results in the movement of a velocity antinode (pressure node) towards this location. For the plenum mode seen in Fig. 6, this has the effect of moving the pressure node in the plenum further downstream towards the reference location and effectively increasing the wavelength of this mode or decreasing the frequency. The trend is reversed for the chamber mode since the pressure node is found downstream of the flame which traverses upstream as n increases (not shown).

The lower sensitivity of the modes to changes in n at higher $|\mathcal{R}_{out}|$ is because the flame is located close to pressure nodes for these reflection coefficients and therefore the flame dynamics becomes decoupled as seen in Ref. [31]. A surprising observation in Fig. 8 is the destabilisation of modes with decreasing $\mathcal{R}_{out}$ or increasing acoustic losses at the outlet boundary. This counter-intuitive observation is consistent with a recent study [32] where it was concluded that decreasing reflection coefficient at the outlet boundary does not necessarily imply stabilisation of the system.

4.1 Beating phenomenon

It is worth revisiting the beating phenomena with the insights gathered on the two independent frequencies excited for case 1b and 2b. As seen in Fig. 3 for cases 1b and 2b, in addition to the two acoustic modes at f_o and f_1 linear combinations of these two frequencies are also excited. This is the result of the quadratic and cubic nonlinearities due to flame dynamics. It is straightforward to see that flame dynamics with $\dot{Q}' \propto \dot{p}'^2$ and $\dot{Q}' \propto \dot{p}'^3$ can generate these additional frequencies after substituting the ansatz $p' \sim \sum_{i=0}^{1} |\hat{p}_i| \exp(i\omega_i t)$.

The cubic nonlinearity is a result of the saturation mechanism of flame dynamics called *kinematic restoration* [33–35]. This refers to the ability of an anchored flame to restore its equilibrium position after being disturbed by an acoustic influx of momentum. Mathematically, this physical mechanism is sufficiently represented by cubic nonlinearities and its combined action with acoustic boundary losses has the effect of limiting the amplitudes of linarly unstable modes to a finite value. In addition to kinematic restoration, the influx of acoustic disturbance results in an increase in flame surface/volume. In general, the time scales at which kinematic restoration and increase in flame surface/volume happens are not equal [14, 35]. This difference in the two time scales results in an asymmetry in the positive and negative fluctuation of $\dot{Q}$ which is accurately represented by quadratic nonlinearities [25].

At any point within the geometry upstream $(u - \overline{c})$ and downstream $(u + \overline{c})$ travelling waves superpose resulting in a standing wave pattern. In cases 1b and 2b, the same process occurs albeit at two independent frequencies f_o and f_1 in addition to their linear combinations. Since the two unstable acoustic mode frequencies are not closely spaced, the resulting standing wave pattern generated from superposition between acoustic waves oscillating at only f_o and f_1 would not be akin to those seen in Fig. 2. This is illustrated in Fig. 9b using synthetic signals given by

$$A = \sin\{f_0 t\} + \sin\{f_1 t\}, \tag{9}$$

$$B = 0.1 \times A + \sin\{(f_0 + f_1)\, t\} + \sin\{(f_0 - f_1)\, t\}. \tag{10}$$

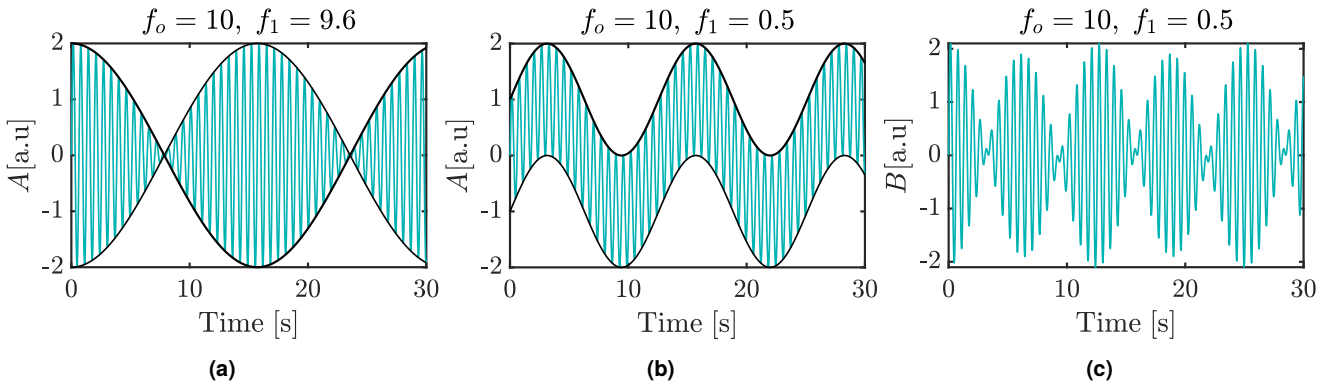

FIGURE 9: SYNTHETIC SIGNALS ILLUSTRATING BEATING PHENOMENON.

Note that signal B may be composed of other linear combinations of frequencies which are omitted here in the interest of brevity.

Closely spaced mode not seen in this work, however, would generate a beating pattern similar (see Fig. 9a) to Fig. 2 for cases 1b and 2b. The significance of the additional acoustic waves generated at frequencies which are linear combinations of f_o and f_1 are illustrated in Fig. 9c which shows the beating pattern similar to this work. The presence of two unstable acoustic modes along with the flame nonlinearities which generate additional acoustic waves are therefore essential in the generation of the beating pattern observed in this work. Beating is not observed for the other cases either because the plenum mode is not destabilised or due to a lower DoF and strength of nonlinearity.

5. CONCLUSIONS

A detailed dynamical characterisation and reduced order model of the thermoacoustics in an LDI hydrogen combustor is presented in this study. The insights gained from the dynamical characterisation and reduced order model will aid the development of a modelling framework to predict instabilities in this combustor. The following are the conclusions of this work:

- A wide variety of probability distributions for pressure amplitude such as normal, bimodal, trimodal and other complex distributions are observed for different cases in the LDI combustor. Some of these distributions are asymmetric about zero amplitude. Based on a past study [25], it is concluded that time-delay, contributions from higher acoustic modes and stochastic forcing are essential features required to model the system dynamics.

- The frequency spectrum reveals a rich variety of unstable modes with significant contributions from higher harmonics, sub-harmonics and incommensurate frequencies. These observations suggest that nonlinearities play a significant role in the dynamics of the system and linearisation is not possible. It is common to model thermoacoustic systems with cubic nonlinearities, but the presence of significant contributions at higher harmonics also highlights the importance of quadratic nonlinearity.

- Poincaré map and correlation dimension are used to qualitatively and quantitatively identify the periodicity and number of DoF of the system. A rich variety of dynamical states such as period-1, period-2, quasi-periodic and chaotic states are identified. This information allows to identify the number of independent equations required to model the system. The significantly high values of correlation dimension for certain cases highlighted the importance of stochastic forcing.

- The spatial structure of the modes are identified using a reduced order linear framework with n–τ flame dynamics. The unstable frequencies found using time series analysis are associated to either a plenum mode or a combination of plenum and chamber modes. Without the aid of a reduced order model, such a classification of the modes and their spatial structure would not have been possible. It is concluded that the quasi-periodic oscillations result from the nonlinear interaction between two incommensurate frequencies associated with a combination of plenum and chamber modes. Since the frequencies are not closely spaced, analysis with simple synthetic signals reveals that the acoustic waves generated by the flame at linear combinations of the two independent frequencies are essential in reproducing the quasi-periodic oscillations.

- Additionally, parametric analysis on thermoacoustic mode eigenvalues show that increasing n increases or decreases the frequency of mode depending on whether it is a chamber or a plenum mode. Modes with lower reflection coefficient are more sensitive to changes in n and surprisingly more unstable, which is consistent with a past study [32].

ACKNOWLEDGMENTS

A. D. K acknowledges the financial support from the Cambridge Trust. The UCAM authors acknowledge the support from MHI, Ltd., Takasago, Japan. The UCL authors would like to acknowledge financial support from UKRI Future Leaders Fellowship (MR/T019735/1) towards this work.

REFERENCES

[1] Yu, G., Law, C. K. and Wu, C. K. “Laminar flame speeds of hydrocarbon + air mixtures with hydrogen addition.” *Combust. Flame* Vol. 63, No. 3 (1986): pp. 339–347. DOI 10.1016/0010-2180(86)90003-9.

[2] Chterev, Ianko and Boxx, Isaac. "Effect of hydrogen enrichment on the dynamics of a lean technically premixed elevated pressure flame." *Combust. Flame* Vol. 225 (2021): pp. 149–159. DOI 10.1016/j.combustflame.2020.10.033.

[3] Indlekofer, Thomas, Ahn, Byeonguk, Kwah, Yi Hao, Wiseman, Samuel, Mazur, Marek, Dawson, James R. and Worth, Nicholas A. "The effect of hydrogen addition on the amplitude and harmonic response of azimuthal instabilities in a pressurized annular combustor." *Combust. Flame* Vol. 228 (2021): pp. 375–387. DOI 10.1016/j.combustflame.2021.02.015.

[4] Schuller, T., Marragou, S., Oztarlik, G., Poinsot, T. and Selle, L. "Influence of hydrogen content and injection scheme on the describing function of swirled flames." *Combust. Flame* Vol. 240 (2022): p. 111974. DOI 10.1016/j.combustflame.2021.111974.

[5] Goldmann, Andreas and Dinkelacker, Friedrich. "Experimental investigation and modeling of boundary layer flashback for non-swirling premixed hydrogen/ammonia/air flames." *Combust. Flame* Vol. 226 (2021): pp. 362–379. DOI 10.1016/j.combustflame.2020.12.021.

[6] Lee, Taesong and Kim, Kyu Tae. "Combustion dynamics of lean fully-premixed hydrogen-air flames in a mesoscale multinozzle array." *Combust. Flame* Vol. 218 (2020): pp. 234–246. DOI 10.1016/j.combustflame.2020.04.024.

[7] Funke, H. H.W., Beckmann, N. and Abanteriba, S. "An overview on dry low NOx micromix combustor development for hydrogen-rich gas turbine applications." *Int. J. Hydrogen Energy* Vol. 44, No. 13 (2019): pp. 6978–6990. DOI 10.1016/j.ijhydene.2019.01.161.

[8] York, William D., Ziminsky, Willy S. and Yilmaz, Ertan. "Development and testing of a low NOx hydrogen combustion system for heavy-duty gas turbines." *J. Eng. Gas Turbines Power* Vol. 135, No. 2. DOI 10.1115/1.4007733/373379.

[9] Marek, C John, Smith, Timothy D and Kundu, Krishna. "Low Emission Hydrogen Combustors for Gas Turbines Using Lean Direct Injection." *41st AIAA/ASME/SAE/ASEE Jt. Propuls. Conf. Exhib. Tucson, Arizona, July 10–13* .

[10] Lieuwen, Timothy C. and Yang, Vigor. *Combustion Instabilities In Gas Turbine Engines: Operational Experience, Fundamental Mechanisms, and Modeling*. American Institute of Aeronautics and Astronautics (2006). DOI 10.2514/4.866807.

[11] Poinsot, Thierry. "Prediction and control of combustion instabilities in real engines." *Proc. Combust. Inst.* Vol. 36, No. 1 (2017): pp. 1–28. DOI 10.1016/j.proci.2016.05.007.

[12] Kumar, Ankit D., Massey, James C., Boxx, Isaac and Swaminathan, Nedunchezhian. "Effects of Hydrogen Enrichment on Thermoacoustic and Helical Instabilities in Swirl Stabilised Partially Premixed Flames." *Flow, Turbul. Combust.* (2023): pp. 1–39DOI 10.1007/s10494-023-00504-4/figures/18.

[13] Kang, Hyebin and Kim, Kyu Tae. "Combustion dynamics of multi-element lean-premixed hydrogen-air flame ensemble." *Combust. Flame* Vol. 233 (2021): p. 111585. DOI 10.1016/j.combustflame.2021.111585.

[14] Kumar, Ankit D., Massey, James C., Stöhr, Michael, Meier, Wolfgang and Swaminathan, Nedunchezhian. "Period-2 Thermoacoustics in a Swirl-Stabilised Partially Premixed Flame Computed Using Large Eddy Simulation." *Flow, Turbul. Combust.* Vol. 111, No. 3 (2023): pp. 995–1028. DOI 10.1007/s10494-023-00452-z/figures/22.

[15] Juniper, Matthew P. and Sujith, R. I. "Sensitivity and Nonlinearity of Thermoacoustic Oscillations." *Annu. Rev. Fluid Mech.* Vol. 50 (2018): pp. 661–689. DOI 10.1146/annurev-fluid-122316-045125.

[16] Kabiraj, Lipika, Sujith, R. I. and Wahi, Pankaj. "Bifurcations of self-excited ducted laminar premixed flames." *J. Eng. Gas Turbines Power* Vol. 134, No. 3. DOI 10.1115/1.4004402/455902.

[17] Kobayashi, Hiroaki, Gotoda, Hiroshi, Tachibana, Shigeru and Yoshida, Seiji. "Detection of frequency-mode-shift during thermoacoustic combustion oscillations in a staged aircraft engine model combustor." *J. Appl. Phys.* Vol. 122, No. 22 (2017): p. 224904. DOI 10.1063/1.5003912/155404.

[18] Kushwaha, Abhishek, Kasthuri, Praveen, Pawar, Samadhan A., Sujith, R. I., Chterev, Ianko and Boxx, Isaac. "Dynamical Characterization of Thermoacoustic Oscillations in a Hydrogen-Enriched Partially Premixed Swirl-Stabilized Methane/Air Combustor." *J. Eng. Gas Turbines Power* Vol. 143, No. 12. DOI 10.1115/1.4052091.

[19] Guan, Yu, Gupta, Vikrant, Wan, Minping and Li, Larry K.B. "Forced synchronization of quasiperiodic oscillations in a thermoacoustic system." *J. Fluid Mech.* Vol. 879 (2019): pp. 390–421. DOI 10.1017/jfm.2019.680.

[20] Li, Larry K.B. and Juniper, Matthew P. "Lock-in and quasiperiodicity in a forced hydrodynamically self-excited jet." *J. Fluid Mech.* Vol. 726 (2013): pp. 624–655. DOI 10.1017/jfm.2013.223.

[21] Zhou, Hao, Tang, Qi, Ren, Tao, Li, Guoneng and Cen, Kefa. "Control of thermoacoustic instabilities by CO2 and N2 jet in cross-flow." *Appl. Therm. Eng.* Vol. 36, No. 1 (2012): pp. 353–359. DOI 10.1016/j.applthermaleng.2011.10.048.

[22] Mensah, Georg A. and Moeck, Jonas P. "Acoustic Damper Placement and Tuning for Annular Combustors: An Adjoint-Based Optimization Study." *J. Eng. Gas Turbines Power* Vol. 139, No. 6. DOI 10.1115/1.4035201/374005.

[23] Mazur, Marek, Nygård, Håkon T., Dawson, James and Worth, Nicholas. "Experimental Study of Damper Position on Instabilities in an Annular Combustor." DOI 10.1115/gt2018-75070.

[24] Ezenwajiaku, Chinonso, Balachandran, Ramanarayanan, Ducci, Andrea, Picciani, Mark and Talibi, Midhat. "Experimental Characterisation of the Dynamics of Partially Premixed Hydrogen Flames in a Lean Direct Injection (LDI) Combustor." *Turbo Expo Power Land, Sea, Air* Vol. 86953 (2023): p. V03at04a073. DOI 10.1115/gt2023-102611.

[25] Bonciolini, Giacomo, Faure-Beaulieu, Abel, Bourquard, Claire and Noiray, Nicolas. "Low order modelling of thermoacoustic instabilities and intermittency: Flame response delay and nonlinearity." *Combust. Flame* Vol. 226 (2021): pp. 396–411. DOI 10.1016/j.combustflame.2020.12.034.

[26] Fraser, Andrew M and Swinney, Harry L. "Independent coordinates for strange attractors from mutual infoiiiiation." Vol. 33, No. 2.

[27] Kennel, Matthew B, Brown, Reggie and Abarbanel, Henry D I. "Determining embedding dimension for phase-space reconstruction using a geometrical construction." *Phys. Rev. A* Vol. 45, No. 6 (1992): pp. 3403–3411.

[28] Launay, Gaby, Cambonie, Tristan, Henry, Daniel, Pothérat, Alban and Botton, Valéry. "Transition to chaos in an acoustically driven cavity flow." *Phys. Rev. Fluids* Vol. 4, No. 4 (2019): p. 044401. DOI 10.1103/physrevfluids.4.044401/figures/19/medium.

[29] Orchini, Alessandro, Silva, Camilo F., Mensah, Georg A. and Moeck, Jonas P. "Thermoacoustic modes of intrinsic and acoustic origin and their interplay with exceptional points." *Combust. Flame* Vol. 211 (2020): pp. 83–95. DOI 10.1016/j.combustflame.2019.09.018.

[30] Crocco, L. "Aspects of Combustion Stability in Liquid Propellant Rocket Motors Part I: Fundamentals. Low Frequency Instability With Monopropellants." *J. Am. Rocket Soc.* Vol. 21, No. 6 (1952): pp. 163–178. DOI 10.2514/8.4393.

[31] Yong, Kah Joon, Silva, Camilo F. and Polifke, Wolfgang. "A categorization of marginally stable thermoacoustic modes based on phasor diagrams." *Combust. Flame* Vol. 228 (2021): pp. 236–249. DOI 10.1016/J.COMBUSTFLAME.2021.01.003.

[32] Yong, Kah Joon, Meindl, Maximilian, Polifke, Wolfgang and Silva, Camilo F. "Thermoacoustic Spectrum of a Swirled Premixed Combustor with Partially Reflecting Boundaries." *J. Eng. Gas Turbines Power* Vol. 142, No. 1. DOI 10.1115/1.4045275/1065988. URL https://dx.doi.org/10.1115/1.4045275.

[33] Preetham, Santosh, H. and Lieuwen, Tim. "Dynamics of Laminar Premixed Flames Forced by Harmonic Velocity Disturbances." *J. Propuls. Power* Vol. 24, No. 6 (2008): pp. 1390–1402. DOI 10.2514/1.35432. URL https://arc.aiaa.org/doi/10.2514/1.35432.

[34] Noiray, Nicolas, Bothien, Mirko and Schuermans, Bruno. "Investigation of azimuthal staging concepts in annular gas turbines." *Combust. Theory Model.* Vol. 15, No. 5 (2011): pp. 585–606. DOI 10.1080/13647830.2011.552636. URL https://www.tandfonline.com/doi/abs/10.1080/13647830.2011.552636.

[35] Blumenthal, Ralf S., Subramanian, Priya, Sujith, R. I. and Polifke, Wolfgang. "Novel perspectives on the dynamics of premixed flames." *Combust. Flame* Vol. 160, No. 7 (2013): pp. 1215–1224. DOI 10.1016/J.COMBUSTFLAME.2013.02.005.

FIGURE CAPTIONS

The following is a list of the figure captions in this paper:

Fig 1: Schematic of the geometry.

Fig 2: Pressure time series and amplitude PDFs at probe-2 for U_b = 30m/s (top two frames) and U_b = 60 m/s (bottom two frames).

Fig 3: Frequency spectrum of SPL at probe-2 for U_b = 30m/s (top frame) and U_b = 60 m/s (bottom frame).

Fig 4: Poincaré section (top frame) and slope of the correlation sum D_c for a range of normalised Euclidean distance $R/R_{\max}$ for U_b = 30 m/s. The filled symbols in the bottom frame correspond to unfiltered signal whereas the open symbols correspond to low pass filtered signal with a suitable cutoff frequency typically of the order of 1000 Hz. The red line denotes the bisectrix and the grey lines denote $p'_{\max}(i) = 0$ and $p'_{\max}(i+1) = 0$ lines.

Fig 5: Figure caption same as Fig. 4 except that it corresponds to case U_b = 60 m/s.

Fig 6: Acoustic pressure mode amplitudes obtained from ROM for case 1b and 2b in the absence of a flame.

Fig 7: Acoustic pressure mode amplitudes obtained from ROM for case 1b and 2b in the the presence of a flame. The white star demarcates the location of the pressure probes.

Fig 8: Thermoacoustic eigenvalue variation with $\mathcal{R}_{\text{out}}$ and n for the plenum and the chamber mode at τ = 0.6 ms.

Fig 9: Synthetic signals illustrating beating phenomenon.

Figure caption for graphical abstract: Acoustic pressure amplitudes for two cases with different bulk mean velocity.